Improving the Representation of Moisture and Convective Instability in Baroclinic-Wave Channel Simulations

DANIEL J. LLOVERAS[a] AND DALE R. DURRAN[a]

[a] *Department of Atmospheric Sciences, University of Washington, Seattle, Washington*

(Manuscript received 14 September 2023, in final form 25 March 2024, accepted 8 April 2024)

ABSTRACT: We present an improved approach to generating moist baroclinically unstable background states for *f*-plane-channel simulations via potential vorticity (PV) inversion. Previous studies specified PV distributions with constant values in the troposphere and the stratosphere, but this produces unrealistic static-stability profiles that decrease sharply with height in the troposphere. Adding moisture to such environments can yield unrealistically large values of convective available potential energy (CAPE) even for reasonable relative humidity (RH) distributions. In our modified approach, we specify a PV distribution that increases with height in the troposphere and the stratosphere, yielding background states with more realistic values of static stability and CAPE. This modification produces environments that are better suited for representing moist processes, namely, deep convection, in idealized extratropical-cyclone simulations. Also, we present a method for introducing moisture that preserves a specified RH distribution while maintaining hydrostatic balance. Our approach allows for a large degree of control over the initial conditions, as background states with different jet strengths and shapes, average temperatures, moisture contents, or horizontal shears can easily be obtained without changing the underlying PV formula and inadvertently producing unreasonable values of static stability or CAPE. We demonstrate the characteristics of idealized extratropical cyclones developing in our background states by adding localized perturbations that represent an upper-level trough passing over a low-level frontal zone. In particular, we illustrate the impacts of horizontal shear, moisture, and grid spacing on baroclinic-wave development.

KEYWORDS: Extratropical cyclones; Baroclinic models; Model initialization

1. Introduction

Idealized baroclinic-wave simulations are valuable tools for studying extratropical-cyclone processes in simplified, controlled environments. A widely used configuration of such simulations is the so-called baroclinic channel, which involves the specification of a baroclinically unstable background state and a perturbation to initiate development in a zonally periodic domain with *f*-plane geometry. Channel simulations have significantly advanced the understanding of dry baroclinic instability by providing more realism and complexity than the Eady (1949) model, but more simplicity and control than real-world simulations with state-of-the-art numerical weather prediction (NWP) models. For example, channel simulations have offered insight into baroclinic life cycles (Davies et al. 1991; Wernli et al. 1998), frontogenesis (Hoskins and West 1979; Rotunno et al. 1994), and gravity waves (Zhang 2004; Plougonven and Snyder 2007).

Moist baroclinic instability can also be examined by introducing moisture to the background state, allowing for the investigation of important phenomena such as latent heat release (Nuss and Anthes 1987; Schemm et al. 2013; Kirshbaum et al. 2018), precipitation patterns (Norris et al. 2014, 2017), kinetic-energy spectra (Waite and Snyder 2013), and predictability (Tan et al. 2004; Zhang et al. 2007; Sun and Zhang 2016; Lloveras et al. 2022, 2023). Careful consideration is necessary when specifying moist background states to ensure that the vertical motions, clouds, and precipitation driven by convective instability are realistic throughout the domain. However, previous methods have specified distributions of static stability, temperature, and moisture that are not suitable for plausibly representing moist convection. The goal of this paper is to present an approach that more realistically incorporates moist processes in *f*-plane-channel simulations of baroclinic instability.

The first step is to define a baroclinically unstable jet in thermal-wind balance with appropriate values of static stability and temperature. There exist three main methods of doing so, but they begin by specifying different atmospheric fields and thereby provide tight control over different aspects of the initial conditions. The method of focus for this paper involves the nonlinear inversion of a specified distribution of Ertel's potential vorticity (PV). The other two methods involve the direct specification of either the zonal wind (Terpstra and Spengler 2015) or the temperature (Olson and Colle 2007). We focus on the PV-inversion approach because it provides control over the static stability via the specification of PV, control over the temperature via the top boundary condition, and control over the baroclinity via the specification of the tropopause. Also, this method has been widely used to initialize simulations of moist baroclinic waves (Tan et al. 2004; Zhang et al. 2007; Waite and Snyder 2013; Sun and Zhang 2016; Norris et al. 2014, 2017; Lloveras et al. 2022, 2023).

For simplicity, the most common choice of PV distribution is one with constant values in the troposphere and stratosphere, with the PV increasing rapidly in a shallow tropopause layer that varies in height from south to north. This configuration can produce reasonable simulations of dry baroclinic instability (Rotunno et al. 1994; Zhang 2004; Menchaca

Corresponding author: Daniel J. Lloveras, lloveras@uw.edu

DOI: 10.1175/MWR-D-23-0210.1

and Durran 2017). However, Lloveras et al. (2022) showed that specifying constant PV in the troposphere causes the buoyancy frequency to decrease sharply with height, leading to unrealistically high values near the surface for plausible values near the tropopause. For convection-permitting channel simulations, this implausible specification of static stability produces vertical motions, clouds, and precipitation that are not representative of real-world extratropical cyclones. Lloveras et al. (2022) modified the PV distribution, with the PV increasing with height in the troposphere, to yield a nearly constant value of buoyancy frequency. They found that this environment produced extratropical cyclones with more plausible moist processes in their convection-permitting simulations.

In addition, if the temperature is not specified appropriately, the convective available potential energy (CAPE) can rise to values that are not representative of the baroclinic atmosphere. For example, Tan et al. (2004, their Fig. 1) specified surface temperatures warmer than 306 K at the southern end of their domain. This temperature specification, combined with the sharp decrease in static stability with height associated with a constant-PV troposphere, produced a moist background state with a domain-maximum CAPE of 6000 J kg^{-1} and values larger than 1000 J kg^{-1} over more than a third of the domain. This unreasonably high degree of convective instability limits the extent to which their moist baroclinic-wave simulations can be used to understand real-world extratropical cyclones.

Finally, when introducing moisture to the background state, the required prognostic variable is the water vapor mixing ratio, but this variable is typically not specified directly. Instead, the most common approach is to define a relative humidity (RH) distribution and compute the mixing ratios corresponding to this distribution. However, since the effect of added moisture on pressure and density (i.e., the virtual-temperature effect) must be accounted for to maintain hydrostatic balance, the actual RH can differ significantly from that initially specified. This is because the temperature distribution used to compute the mixing ratios for the specified RH must change when recomputing hydrostatic balance. Alternatively, the virtual temperature can be specified when computing the initial jet (Terpstra and Spengler 2015; Kirshbaum et al. 2018), but this can also cause problems because the temperature, not the virtual temperature, is required to compute the mixing ratios corresponding to the specified RH. This lack of control over the moisture content can cause complications, especially for studies investigating the sensitivity of baroclinic development to the background-state RH.

In this paper, we document an approach to generating baroclinically unstable background states that are more suitable for simulating moist processes than those produced by previous PV-inversion methods. In particular, we build on the results of Lloveras et al. (2022) by further improving their PV distribution, yielding moist background states with more plausible values of static stability, temperature, and CAPE. We also present a procedure for introducing moisture that preserves a specified RH distribution while maintaining hydrostatic balance. We discuss the generation of the background states in section 2. In section 3, we present illustrative simulations of idealized extratropical cyclones developing in our background states using the Advanced Research version of Weather Research and Forecasting (WRF-ARW) Model (version 3.6.1; Skamarock et al. 2008). We provide a summary in section 4.

2. Generating the moist background states

a. PV inversion procedure

We generate a baroclinically unstable jet in thermal-wind balance by inverting a specified PV distribution following Plougonven and Snyder (2007). This involves solving for the geopotential ϕ in the nonlinear PV equation on the y–Π plane, where the scaled Exner function $\Pi = c_p(p/p_0)^\kappa$ is the vertical coordinate, p is the pressure, $p_0 = 1000$ hPa is the reference pressure, $c_p = 1004\ \mathrm{J\,K^{-1}\,kg^{-1}}$ is the specific heat at constant pressure, $\kappa = R_d/c_p$, and $R_d = 287\ \mathrm{J\,K^{-1}\,kg^{-1}}$ is the ideal gas constant for dry air. We derive the PV equation by expressing Eq. (2.3) from Davis and Emanuel (1991) in two dimensions and with a constant Coriolis parameter $f_0 = 10^{-4}\ \mathrm{s^{-1}}$:

$$\mathrm{PV}(y,\Pi) = \frac{g\kappa c_p^{1/\kappa}}{p_0}\Pi^{1-1/\kappa}\left[f_0\frac{\partial^2\phi}{\partial\Pi^2} + f_0^{-1}\frac{\partial^2\phi}{\partial y^2}\frac{\partial^2\phi}{\partial\Pi^2} - f_0^{-1}\left(\frac{\partial^2\phi}{\partial y\partial\Pi}\right)^2\right]. \tag{1}$$

The numerical details for solving this equation are in appendix C. The boundary conditions involve setting $\partial\phi/\partial y = 0$ at the northern and southern boundaries, $\partial\phi/\partial\Pi$ at the top boundary, and the geopotential at the bottom boundary ϕ_{bot}.

From the solution for ϕ, we compute the geostrophically balanced zonal wind:

$$u = -\frac{1}{f_0}\frac{\partial\phi}{\partial y}, \tag{2}$$

and the hydrostatically balanced moist potential temperature,

$$\theta_m = -\frac{\partial\phi}{\partial\Pi}, \tag{3}$$

where $\theta_m = \theta[1 + (R_v/R_d)q_v]$, θ is the potential temperature, q_v is the water vapor mixing ratio, and $R_v = 461.6\ \mathrm{J\,K^{-1}\,kg^{-1}}$ is the ideal gas constant for water vapor. We use θ_m instead of the virtual potential temperature θ_v, and we use the notation q_v for the water vapor mixing ratio to follow the convention of the WRF Model (Skamarock et al. 2008, their section 2.3). The balance conditions mean that $u = 0\ \mathrm{m\,s^{-1}}$ at the northern and southern boundaries, the top moist potential temperature $\theta_{m_{\mathrm{top}}}$ sets $\partial\phi/\partial\Pi$ at the top boundary, and ϕ_{bot} sets the amount of horizontal shear at the bottom boundary.

The domain has a north–south extent of $L_y = 7200$ km and 180 evenly spaced Π levels varying from $\Pi_{\mathrm{bot}} = 1008\ \mathrm{J\,K^{-1}\,kg^{-1}}$ to $\Pi_{\mathrm{top}} = 424\ \mathrm{J\,K^{-1}\,kg^{-1}}$. These bottom and top Π values correspond to pressures of about 1014 and 50 hPa, respectively, resulting in a vertical domain extending to about 20 km.

TABLE 1. Parameters that can be modified to obtain different baroclinically unstable background states without altering the underlying PV formula.

Parameter name	Parameter description	Our value	Consequence of increasing
$\Delta\Pi_{ns}$	North–south variation in tropopause height	30 J K^{-1} kg^{-1}	Jet strength increases
Δy_{π}	North–south extent of tropopause height variation	1000 km	Jet width increases and strength decreases
Π_a	Average tropopause height	680 J K^{-1} kg^{-1}	Tropopause lowers
θ_{m_a}	Average moist potential temperature at top boundary	535 K	Domain-wide temperature increases
RH_0	Surface RH	0.85	Domain-wide moisture content increases
Δu_{ns}	Max additional zonal wind for barotropic shear	10 m s^{-1}	Barotropic-shear strength increases
$\Delta\phi_{ns}$	Max difference in bottom geopotential for low-level shear	1500 m^2 s^{-2}	Low-level-shear strength increases

b. *Specifying the PV, tropopause, and boundary conditions*

The PV distribution increases with height in the troposphere, in a shallow tropopause layer, and in the stratosphere. The PV formula, provided in appendix B, is a function of Π and the tropopause height $\Pi_{tp}(y)$, which controls the jet height, shape, and strength and is given by

$$\Pi_{tp}(y) = \begin{cases} \Pi_a - \Delta\Pi_{ns}, & \text{if } \tilde{y}_{\pi} < -\dfrac{\pi}{2}, \\ \Pi_a + \Delta\Pi_{ns}\sin(\tilde{y}_{\pi}), & \text{if } -\dfrac{\pi}{2} \le \tilde{y}_{\pi} \le \dfrac{\pi}{2}, \\ \Pi_a + \Delta\Pi_{ns}, & \text{if } \tilde{y}_{\pi} > \dfrac{\pi}{2}, \end{cases} \tag{4}$$

where $\tilde{y}_{\pi} = 1.5(y - L_y/2)/\Delta y_{\pi}$. The first three rows in Table 1 define the parameters in this formula, provide our values, and explain what happens to the jet when they are increased.

The top boundary condition uses the same functional form as the tropopause:

$$\theta_{m_{top}}(y) = \begin{cases} \theta_{m_a} - \Delta\theta_{m_{ns}}, & \text{if } \tilde{y}_{\theta} < -\dfrac{\pi}{2}, \\ \theta_{m_a} + \Delta\theta_{m_{ns}}\sin(\tilde{y}_{\theta}), & \text{if } -\dfrac{\pi}{2} \le \tilde{y}_{\theta} \le \dfrac{\pi}{2}, \\ \theta_{m_a} + \Delta\theta_{m_{ns}}, & \text{if } \tilde{y}_{\theta} > \dfrac{\pi}{2}, \end{cases} \tag{5}$$

where $\Delta\theta_{m_{ns}} = 10$ K is the difference in $\theta_{m_{top}}$ between the northern and southern boundaries, $\tilde{y}_{\theta} = 1.5(y - L_y/2)/\Delta y_{\theta_m}$, and $\Delta y_{\theta_m} = 1000$ km is the scale for the north–south variation in $\theta_{m_{top}}$. The fourth row of Table 1 explains that θ_{m_a} controls the domain-wide temperature. Adjusting this parameter is particularly useful when working to obtain appropriate surface temperatures.

The simplest choice for the bottom boundary condition is $\phi_{bot} = 0$ m^2 s^{-2}, which produces an environment with zero low-level horizontal shear and a constant surface pressure corresponding to the pressure at Π_{bot} (about 1014 hPa). We call this the "neutral shear" background state. In section 2d, we provide a formula for ϕ_{bot} that produces strong low-level horizontal shear, and we discuss how barotropic shear can be added to the background state.

Figure 1a depicts a vertical cross section of the neutral shear background state. The tropopause height varies from about 11 km at the southern end of the domain to about 8 km at the northern end. This results in a jet height of about 9.5 km and a maximum zonal-wind speed of about 37 m s^{-1}. The surface temperature varies from about 295 to 263 K.

Different jets can be easily obtained by adjusting Π_{tp}, $\theta_{m_{top}}$, and ϕ_{bot}, but we do not recommend modifying the underlying PV formula in (B1) because even minor changes can significantly alter the profiles of static stability, which are very realistic with our formula. This realism is shown by Fig. 2, which depicts vertical profiles of PV and squared moist buoyancy frequency $N_m^2 = (g/\theta_m)(\partial\theta_m/\partial z)$, where $g = 9.81$ m s^{-2} is the gravitational constant and z is the height (m). The profiles correspond to the northern and southern sides of the jet (indicated by the blue and orange dashed lines, respectively, in Fig. 1a).

The (moist) Ertel PV is PV $= (\zeta_a \cdot \nabla\theta_m)/\rho$, where ζ_a is the absolute vorticity. So, assuming that vertical gradients in ζ_a are negligible, if the PV does not vary with height, then $\partial\theta_m/\partial z$ must decrease with height because ρ decreases with height. Since θ_m increases with height, this means that N_m^2 must decrease with height in a constant-PV layer. This can yield highly unrealistic buoyancy-frequency profiles in the troposphere, with values ranging from 2.25×10^{-4} s^{-2} near the surface to 1×10^{-4} s^{-2} in the upper troposphere (Lloveras et al. 2022, their Fig. 1).

In contrast, our PV distribution increases with height in the troposphere (Fig. 2a). This causes $\partial\theta_m/\partial z$ to increase with height at a rate that offsets the increase in θ_m with height, so the buoyancy frequency does not vary strongly with height; N_m^2 is approximately 1×10^{-4} s^{-2} in the lower troposphere and increases gradually with height in the upper troposphere (Fig. 2b). Environments with nearly constant buoyancy frequency in the troposphere are more suitable for simulating plausible vertical motions and clouds than those in which the buoyancy frequency decreases strongly with height over the full depth of the troposphere (Lloveras et al. 2022, their Fig. 4).

We also modify the PV distribution from Lloveras et al. (2022, their appendix A) to produce more realistic buoyancy-frequency profiles in the tropopause layer and in the stratosphere. In particular, our PV distribution increases more rapidly in the tropopause layer, so N_m^2 increases sharply from about 1.5×10^{-4} s^{-2} at the top of the troposphere to just under 8×10^{-4} s^{-2} at the bottom of the stratosphere. In addition, our PV increases more rapidly with height in the stratosphere. This causes N_m^2 to drop off rapidly in the lower stratosphere before reaching a constant value of about 4×10^{-4} s^{-2} starting at about 16 km, a behavior that is very similar to that determined

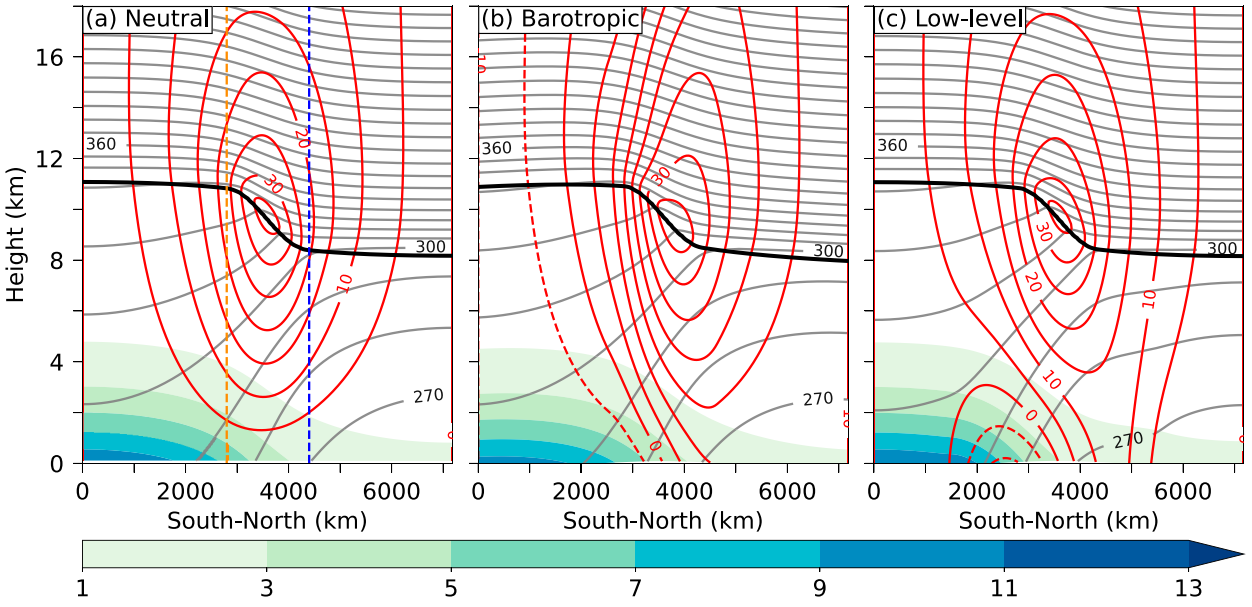

FIG. 1. (a) South–north vertical cross section of the neutral-shear background state for zonal wind u (red contours every 5 m s^{-1}; dashed contours are negative), moist potential temperature θ_m (gray contours every 10 K), and water vapor mixing ratio q_v (color fill every 2 g kg^{-1}). The 2-PVU solid black curve represents the tropopause. The orange and blue dashed lines correspond to the locations of the vertical profiles in Fig. 2. (b) As in (a), but for the background state with barotropic anticyclonic shear. (c) As in (a), but for the background state with low-level anticyclonic shear in the region of strongest baroclinity.

from observations in the wintertime midlatitudes (Birner et al. 2002, denoted by the black dashed curve in Fig. 2b).

c. *Specifying moisture*

We use a regula-falsi (or false-position) method to compute the water vapor mixing ratios for moist simulations that preserve a specified RH distribution while maintaining hydrostatic balance. The hydrostatically balanced θ_m from the PV inversion provides the first guess θ_1 for the potential temperature. Then, we use the formula from Bolton (1980) to estimate the saturation vapor pressure (hPa) corresponding to θ_1:

$$e_{s_1} = 6.112 \exp\left[17.67\left(\frac{T_1 - 273.15}{T_1 - 29.65}\right)\right], \tag{6}$$

where $T_1 = \theta_1(p/p_0)^{\kappa}$. The first guess for the water vapor mixing ratio is then

$$q_{v_1} = \mathrm{RH}\frac{R_d}{R_v}\left(\frac{e_{s_1}}{p - e_{s_1}}\right). \tag{7}$$

We close the loop by updating the potential temperature as $\theta_2 = \theta_m/[1 + (R_v/R_d)q_{v_1}]$ and iterate by using θ_2 to compute e_{s_2} and q_{v_2} with (6) and (7). Though we do not employ a convergence criterion, we find that 10 iterations result in q_v and θ values that almost exactly correspond to the specified RH distribution. The p and θ_m values do not change, so this method does not require the reestablishment of hydrostatic balance.

To clearly demonstrate the efficacy of our method, we specify a horizontally homogeneous RH distribution that decays with height:

$$\mathrm{RH}(z) = \begin{cases} \mathrm{RH}_0[1 - 0.9(z/z_r)^{1.25}], & \text{if } z < z_r, \\ 0.1, & \text{otherwise,} \end{cases} \tag{8}$$

where $\mathrm{RH}_0 = 0.85$ is the surface RH and $z_r = 8$ km is the vertical decay scale.

Figure 3a shows south–north distributions of surface RH at different iterations of our method. The RH values are unrealistically large after one iteration, especially in the southern portion of the domain. This is because e_{s_1} corresponds to the saturation vapor pressure for an environment in which θ equals θ_m, and thus, the q_{v_1} values are too large for the specified RH. The second iteration overcorrects this and is subsequently overcorrected by the third iteration, but by the tenth iteration the actual RH is almost exactly equal to the specified RH of 85%. This RH distribution produces q_v values that reach a maximum of about 13 g kg^{-1} at the surface at the southern boundary and decrease with height and toward the north (Fig. 1a).

Figure 3b shows that the convective instability of our moist background state is reasonable for our specified RH, with a domain-maximum CAPE of 447 J kg^{-1} at the southern boundary that decreases smoothly to 0 J kg^{-1} by $y = 2800$ km. This is in stark contrast to the 6000 J kg^{-1} of CAPE in previous studies that used environments with constant-PV tropospheres and much warmer temperatures (Tan et al. 2004; Zhang et al. 2007; Sun and Zhang 2016). The convective instability of their simulations is unreasonably high despite the fact

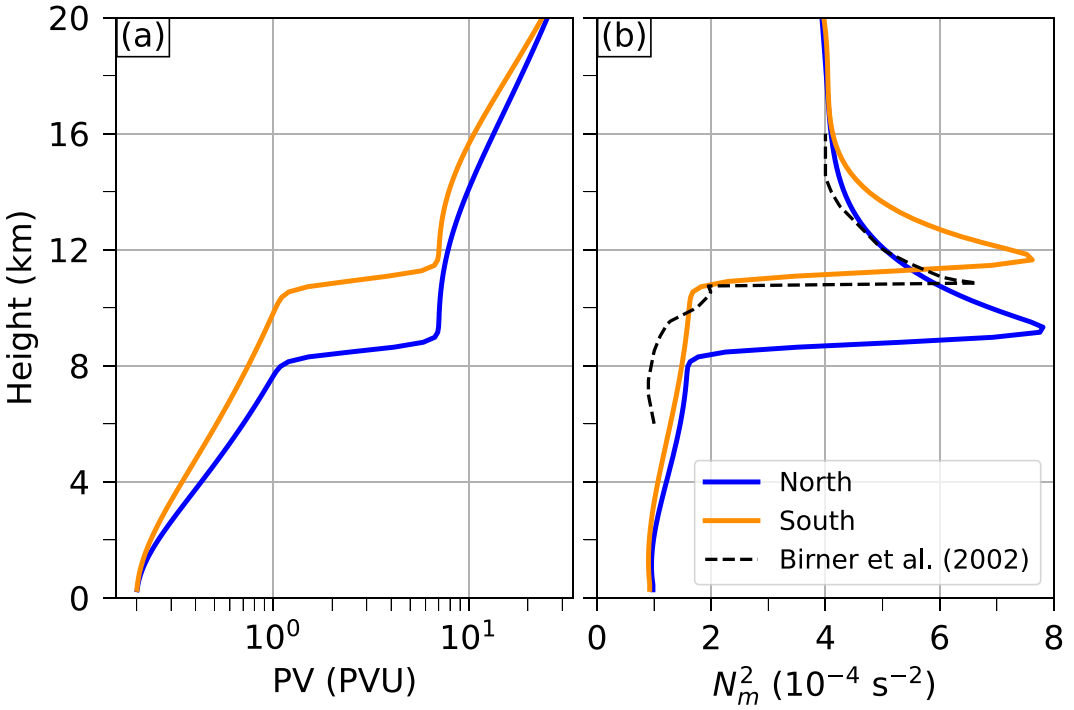

FIG. 2. Vertical profiles of (a) PV (PVU; note the logarithmic scale) and (b) squared moist buoyancy frequency N_m^2 (10^{-4} s^{-2}) at the northern (blue) and southern (orange) sides of the jet. Profiles are computed at $y = 4200$ km for the northern side and $y = 3000$ km for the southern side (corresponding to the dashed blue and orange lines in Fig. 1a, respectively). The black dashed curve in (b), adapted from Fig. 1b in Birner et al. (2002), depicts tropopause-relative observations of the squared buoyancy frequency over Munich, Germany, averaged over 10 years during December, January, and February.

that, at the southern boundary, their surface RH of 50% is much smaller than our 85%.

Our method is effective because it adjusts q_v and θ so that they correspond to the specified RH without requiring the recomputation of hydrostatic balance. This behavior is independent of the specified RH, so our method can be used for any modification to the distribution given by (8). The most simple modification involves changing the surface value RH_0, as noted on the fifth row of Table 1. In appendix A, we discuss how changes to RH_0 can affect baroclinic development. Alternatively, environments with different moisture contents can be obtained for the same RH by modifying the temperature with θ_{m_a}. However, careful attention is required when modifying this parameter to ensure that the CAPE values remain reasonable.

d. Obtaining environments with strong horizontal shear

The environmental horizontal wind shear plays an important role in the structure and development of a baroclinic wave. In a seminal paper, Thorncroft et al. (1993) identified two types of baroclinic-wave life cycles using idealized simulations on the sphere. For the first life cycle (LC1), the environment is characterized by a symmetric jet (i.e., without additional horizontal shear), and baroclinic development is characterized by backward-tilted, elongated troughs that break anticyclonically. For the second life cycle (LC2), cyclonic barotropic shear is added to the jet, resulting in baroclinic development characterized by forward-tilted, broad troughs that break cyclonically.

In contrast to baroclinic-wave simulations on the sphere, *f*-plane-channel simulations typically exhibit LC2-like behavior in the absence of any additional shear, whereas LC1-like behavior can be obtained by adding anticyclonic barotropic shear (Balasubramanian and Garner 1997). Alternatively, Plougonven and Snyder (2007) used the PV-inversion approach for their simulations and found that setting $\phi_{\text{bot}} = 0$ m^2 s^{-2} (as in our neutral-shear case) produced LC2-like behavior, whereas specifying ϕ_{bot} to produce anticyclonic shear only at low levels yielded LC1-like behavior. This approach has the advantage of preserving the specified PV distribution, but has the disadvantage of altering the baroclinity. We consider both approaches for adding anticyclonic shear to obtain LC1-like behavior.

For the "barotropic-shear" background state, a vertically uniform zonal-wind field is added to the environmental flow of the form:

$$u_{\text{bar}}(y) = \begin{cases} -\Delta u_{\text{ns}}, & \text{if } \tilde{y}_u < -\dfrac{\pi}{2}, \\ \Delta u_{\text{ns}} \sin(\tilde{y}_u), & \text{if } -\dfrac{\pi}{2} \le \tilde{y}_u \le \dfrac{\pi}{2}, \\ \Delta u_{\text{ns}}, & \text{if } \tilde{y}_u > \dfrac{\pi}{2}, \end{cases} \tag{9}$$

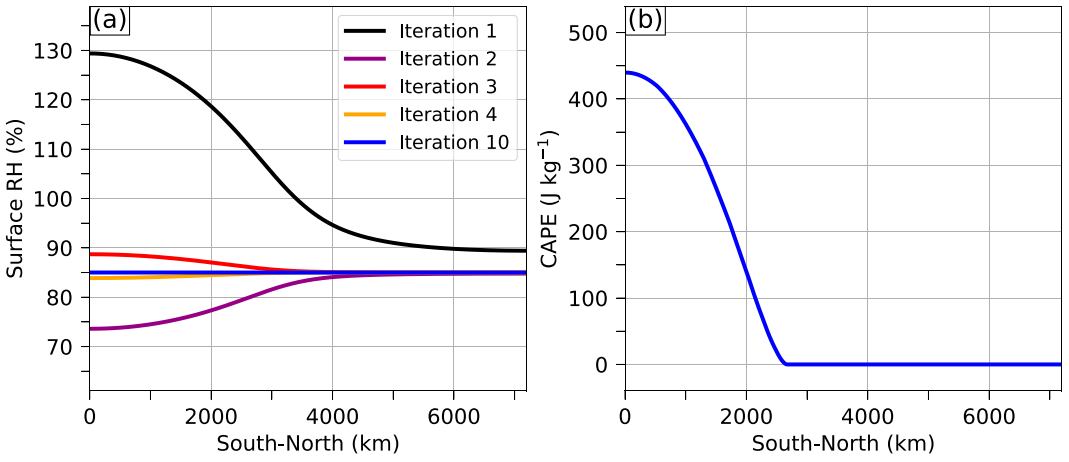

FIG. 3. South–north distributions of (a) surface RH (%) after the first (black), second (purple), third (red), fourth (orange), and tenth (blue) iterations of our method for specifying moisture and (b) surface-based CAPE (J kg^{-1}) after the tenth iteration for the neutral-shear environment.

where $\tilde{y}_u = 1.5(y - L_y/2)/\Delta y_u$ and $\Delta y_u = 1000$ km is the scale for the north–south variation in $u_{\rm bar}$. The sixth row of Table 1 explains that $\Delta u_{\rm ns}$ controls the barotropic-shear strength. The green curve in Fig. 4a shows the south–north structure of this anticyclonically sheared additional wind.

Upon adding $u_{\rm bar,}$ we recompute ϕ to be in geostrophic balance with the modified u. Since the shear is barotropic, this rebalancing does not modify the vertical gradient of ϕ, so θ_m does not change. The green curve in Fig. 4b shows how the shear changes $\phi_{\rm bot}$, which is set to zero in the PV inversion. We recompute geostrophic balance by integrating outward from the center of the domain, so $\phi_{\rm bot} = 0$ m^2 s^{-2} in the center and is less than -3000 m^2 s^{-2} at the northern and southern ends. Recalling that $\phi_{\rm bot}$ corresponds to the geopotential at $\Pi_{\rm bot}$, the domain-average surface pressure would be much smaller than in the neutral-shear environment (about 1014 hPa everywhere) if we used the same $\Pi_{\rm bot}$. So, we set $\Pi_{\rm bot} = 1012.5$ J K^{-1} kg^{-1} for the barotropic-shear case, resulting in surface-pressure values varying from about 1030 hPa in the center of the domain to about 990 hPa at the northern and southern boundaries.

For the "low-level-shear" background state, the PV is inverted with the bottom boundary condition:

$$\phi_{\rm bot}(y) = \begin{cases} \Delta\phi_{\rm ns}\cos(\tilde{y}_\phi)/2, & \text{if } -\pi \le \tilde{y}_\phi \le \pi, \\ -\Delta\phi_{\rm ns}, & \text{otherwise,} \end{cases} \tag{10}$$

where $\tilde{y}_\phi = 1.5(y - L_y/2)/\Delta y_\phi$ and $\Delta y_\phi = 1000$ km is the scale for the north–south variation in $\phi_{\rm bot}$. The seventh row of Table 1 explains that $\Delta\phi_{\rm ns}$ controls the low-level-shear strength. The orange curve in Fig. 4b shows the south–north structure of this $\phi_{\rm bot}$.

This specification of $\phi_{\rm bot}$ results in a $u_{\rm bot}$ field that varies from -11.3 to $+11.3$ m s^{-1} in the center of the domain and

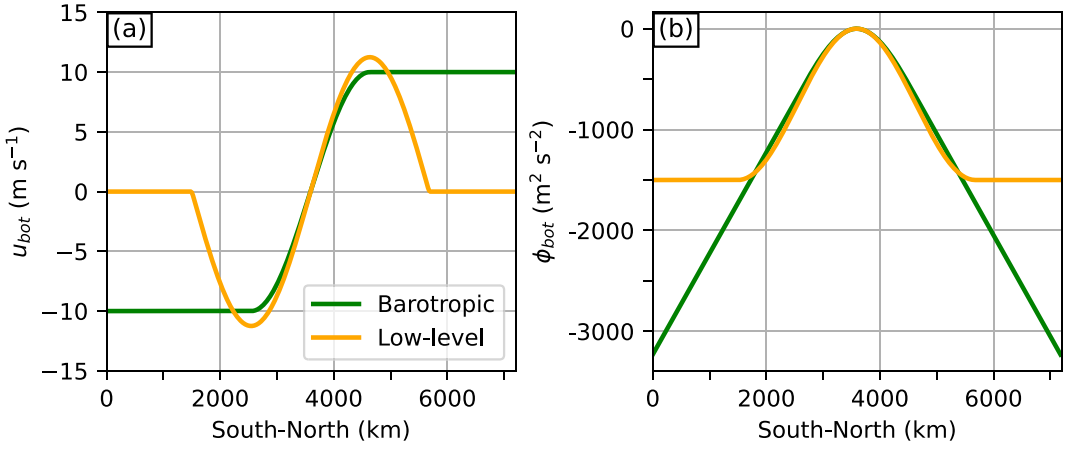

FIG. 4. (a) South–north distributions of zonal wind at the bottom boundary $u_{\rm bot}$ (m s^{-1}) for the environments with barotropic (green) and low-level (orange) anticyclonic shear. (b) As in (a), but for the geopotential at the bottom boundary $\phi_{\rm bot}$ (m^2 s^{-2}).

relaxes to zero at the northern and southern boundaries (orange curve in Fig. 4a). This structure is similar to that of Plougonven and Snyder (2007), which they chose because it does not require a separate lateral boundary condition for the PV inversion (recall that $u = 0$ m s^{-1} at the northern and southern boundaries). This leads to not only anticyclonic shear in the center of the domain but also cyclonic shear at both the northern and southern ends. Similar to the modification in the barotropic-shear environment, we set $\Pi_{\text{bot}} = 1011.5$ J K^{-1} kg^{-1} so that the domain-average surface pressure is more comparable to that of the neutral-shear environment. In the low-level-shear environment, the surface pressure varies from about 1025 hPa in the center to about 1006 hPa at the northern and southern boundaries.

Figures 1b and 1c show vertical cross sections of the barotropic- and low-level-shear background states, respectively. The anticyclonic barotropic shear shifts the jet toward the northern side of the domain but does not modify the baroclinity. The low-level shear is strongest at the surface and decreases with height, so it modifies the baroclinity (e.g., see the distortions in the 270-K contour) but leaves the upper levels mostly unchanged.

3. Illustrative simulations with the WRF Model

The goal of this section is to demonstrate the characteristics of idealized extratropical cyclones developing in the neutral-, barotropic-, and low-level-shear environments, with a particular focus on their sensitivities to the presence of moisture and convective parameterization.

a. Cyclogenetic perturbations

We trigger cyclogenesis by adding localized quasigeostrophic PV (QGPV) perturbations to the background state, an approach used by several recent studies (Menchaca and Durran 2017; Kirshbaum et al. 2018; Lloveras et al. 2022, 2023). The QGPV-inversion method, which uses z as the vertical coordinate, is presented in appendix D. The three-dimensional variables obtained from the QGPV inversion are the pressure perturbation p', the geostrophically balanced zonal- and meridional-wind perturbations u' and v', and the hydrostatically balanced moist-potential-temperature perturbation θ'_m.

Since the QGPV inversion is separate from the specification of the background state, there is a large amount of freedom in defining the cyclogenetic perturbations. We add two QGPV perturbations to the background state: an internal QGPV perturbation situated in the upper troposphere and a thermal perturbation at the bottom boundary that leads to a local tightening of the surface-temperature gradient. These perturbations represent Petterssen's "type-B" cyclogenesis in which an upper-level trough moves over a low-level frontal zone (Petterssen and Smebye 1971).

The upper-tropospheric perturbation is of the form:

$$q'(x, y, z) = q_0 \cos r_{\text{up}} \cos r_z, \tag{11}$$

where $q_0 = 1.25 \times 10^{-4}$ s^{-1}, $r_{\text{up}} = \{[(x - x_{\text{up}})/\delta_{x_{\text{up}}}]^2 + [(y - y_{\text{up}})/\delta_{y_{\text{up}}}]^2\}^{1/2}$, and $r_z = |(z - z_{\text{up}})/\delta_z|$. The horizontal decay scales are $\delta_{x_{\text{up}}} = 200$ km and $\delta_{y_{\text{up}}} = 600$ km, and the vertical decay scale is $\delta_z = 1.5$ km. The parameters r_{up} and r_z are capped at $\pi/2$. The center of the perturbation is at $(x_{\text{up}}, y_{\text{up}}, z_{\text{up}}) = (2800$ km, 3300 km, 8 km).

The moist potential temperature perturbation at the surface is of the form:

$$\theta'_{m_{\text{bot}}}(x, y) = \theta_0 \cos r_{\text{bot}}, \tag{12}$$

where $\theta_0 = 4$ K and $r_{\text{bot}} = \{[(x - x_{\text{bot}})/\delta_{x_{\text{bot}}}]^2 + [(y - y_{\text{bot}})/\delta_{y_{\text{bot}}}]^2\}^{1/2}$, with r_{bot} capped at $\pi/2$. The decay scales are $\delta_{x_{\text{bot}}} = 600$ km and $\delta_{y_{\text{bot}}} = 200$ km, and the perturbation center is southeast of the upper-tropospheric perturbation at $(x_{\text{bot}}, y_{\text{bot}}) = (4000$ km, 2700 km).

Figure 5a shows a west–east vertical cross section of the meridional-wind and pressure perturbations induced by the QGPV perturbations. Both the upper-tropospheric and surface-based perturbations are characterized by pressure perturbations of around −5 hPa and geostrophically balanced cyclonic circulations with maximum wind speeds of about 5 m s^{-1}, although the upper-tropospheric perturbation is stronger and has a larger vertical depth. Figure 5b shows the superposition of the QGPV perturbations on the neutral-shear background state, demonstrating that the upper-tropospheric perturbation produces a shortwave trough at 250 hPa and the surface perturbation produces a local tightening of the surface-temperature gradient.

b. Model configuration

We run three WRF simulations in each of the shear environments: a dry run with a horizontal grid spacing of $\Delta x = 20$ km, a moist run with $\Delta x = 20$ km, and a moist run with $\Delta x = 4$ km. For the moist simulations, our focus is on background states with surface RH values of 85%, but in appendix A we discuss how changes to RH can affect baroclinic development.

The f-plane-channel domain for the WRF simulations has a horizontal extent of $L_x = 8000$ km by $L_y = 7200$ km. The lateral boundary conditions are periodic at the eastern and western boundaries and symmetric (i.e., free slip) at the rigid-wall northern and southern boundaries. We integrate the model for 8 days on a staggered Cartesian Arakawa C grid with third-order Runge–Kutta (RK3) time differencing. The time step is 100 s for the 20-km simulations and 20 s for the 4-km simulations. The acoustic time step is 1/4 of the RK3 time step.

The vertical coordinate for WRF is

$$\eta = \frac{p_h - p_{h_{\text{top}}}}{p_{h_{\text{bot}}} - p_{h_{\text{top}}}}, \tag{13}$$

where p_h is the hydrostatic pressure, $p_{h_{\text{top}}}$ is the hydrostatic pressure at the model top, and $p_{h_{\text{bot}}}$ is the hydrostatic surface pressure. We use 101 staggered vertical levels, defined such that for $k = 0, 1, \ldots, 100$:

$$\eta(k) = \frac{(e^{-2k/100} - e^{-2})}{(1 - e^{-2})}. \tag{14}$$

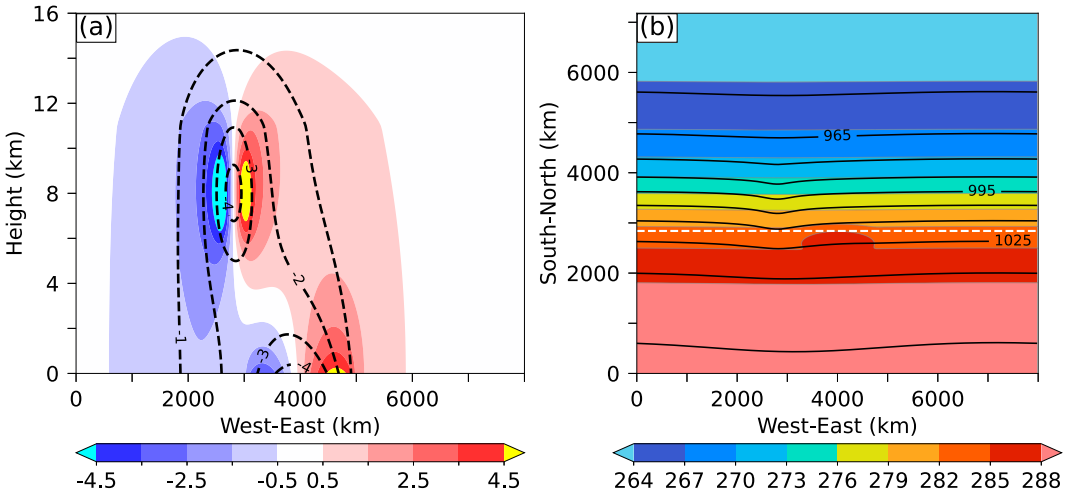

FIG. 5. (a) West–east vertical cross section of the meridional-wind perturbations v' (color fill every 1 m s^{-1}) and pressure perturbations p' (dashed black contours every 1 hPa) obtained from the inversion of the upper-tropospheric and surface QGPV perturbations. (b) Superposition of the QGPV perturbations on the surface potential temperature (color fill every 2 K) and 250-hPa geopotential height (black contours every 10 dam) in the neutral-shear environment. The dashed white line shows the location of the cross section in (a).

This yields vertical levels that are approximately evenly spaced in z in the troposphere and become further apart in the stratosphere.

Since we compute the background state with Π as the vertical coordinate and the cyclogenetic perturbations with z as the vertical coordinate, we must interpolate these fields onto the appropriate η levels before adding them together. This interpolation procedure is common in the initialization of f-plane-channel simulations (e.g., Olson and Colle 2007) because it allows the initial conditions to be used in any mesoscale model provided that the vertical levels for the model are known. In the case of WRF, the interpolation is straightforward for the neutral-shear background state, as the Π levels correspond to exact pressure levels, and the pressure is constant both at the surface and at the model top. For the neutral-shear case, we set $p_{h_{\text{bot}}} = 1014$ hPa and $p_{h_{\text{top}}} = 50$ hPa and interpolate the background-state variables onto the p_h levels obtained from (13). For the barotropic- and low-level-shear cases, we adjust $p_{h_{\text{bot}}}$ and $p_{h_{\text{top}}}$ to be in geostrophic balance with the horizontal shear at the boundaries to obtain the p_h values corresponding to the appropriate η levels. Similarly, interpolating the cyclogenetic perturbations requires $p_{h_{\text{bot}}}$ to be updated by adding the pressure perturbation at the bottom boundary.

For each simulation, model physics include the Yonsei University (YSU) planetary boundary layer scheme (Hong et al. 2006), the revised surface-layer scheme based on the Fifth-generation Pennsylvania State University–National Center for Atmospheric Research Mesoscale Model (MM5) parameterization (Jiménez et al. 2012) with the default roughness of $z_0 = 0.01$ m (there are momentum fluxes, but no heat or moisture fluxes), and the Rayleigh damping scheme from Klemp et al. (2008) in the top 5 km of the model to minimize gravity wave reflections off the top boundary. For the moist simulations, we use the National Severe Storms Laboratory's (NSSL) two-moment microphysics scheme (Mansell et al. 2010). For the 20-km moist simulations, we use the Kain–Fritsch cumulus parameterization (Kain 2004). We do not use cumulus parameterization for the 4-km moist simulations. The 4-km grid spacing, although too coarse to completely resolve convective updrafts, is sufficient to represent much of the structure and evolution of convective systems, and it is well within the range of grid spacings used in typical convection-permitting simulations (Weisman et al. 1997).

The background states undergo small adjustments when evolved in the compressible, nonhydrostatic WRF Model, even in the absence of moisture or QGPV perturbations. This behavior has been noted by other studies that used the PV-inversion method to generate baroclinically unstable background states for f-plane-channel simulations (Plougonven and Snyder 2007; Sun and Zhang 2016). As in these studies, we reduce the artificial oscillations by time-averaging all of the fields over 36-h periods before adding moisture and the cyclogenetic perturbations. Figure 6 shows that before averaging, the neutral-shear background state produces $O(0.5)$ Pa oscillations in surface pressure, and one round of averaging reduces these oscillations by over an order of magnitude.

Also, we employ the Boussinesq approximation in the QGPV inversion, so the cyclogenetic perturbations are not in complete balance with the WRF Model. Since these perturbations are localized, the initial imbalances radiate away as gravity waves. This is in contrast to the artificial oscillations associated with the background state, which persist throughout the simulation and across the entire domain.

c. Cyclone evolution

Here, we examine the baroclinic development in our nine example simulations. Figure 7 shows the evolution of cyclone intensity, measured as the minimum surface-pressure perturbation

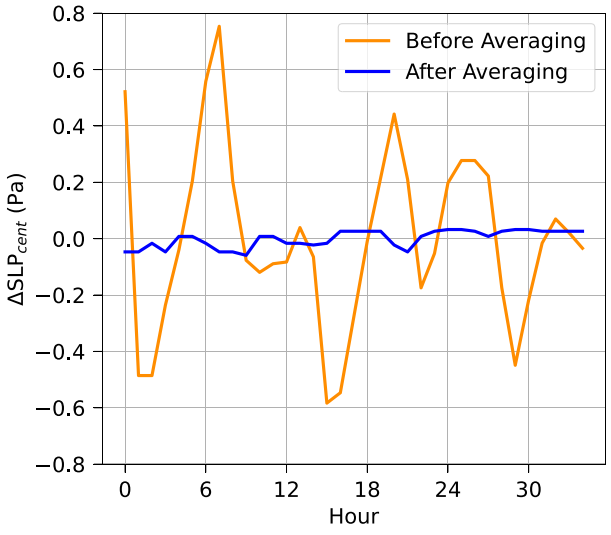

FIG. 6. Time series of the deviation in surface pressure from the time mean at the center of the domain ΔSLP_{cent} (Pa) before (orange) and after (blue) averaging over the 36-h period for the neutral-shear background state.

relative to the zonally uniform background state $(\Delta SLP)_{min}$. For each configuration of moisture and horizontal grid spacing, the cyclone developing in the neutral-shear environment (Fig. 7a) deepens faster than the respective cyclone developing in the barotropic-shear environment (Fig. 7b). This is consistent with previous studies that investigated the impact of anticyclonic barotropic shear on the rate of dry cyclogenesis (Davies et al. 1991; Wernli et al. 1998). In the low-level-shear environment (Fig. 7c), the rate of cyclogenesis is similar to the barotropic-shear environment in each configuration of moisture and horizontal grid spacing through the first 4 days. After day 5, however, the cyclones in the low-level-shear environment deepen faster, eventually reaching values of $(\Delta SLP)_{min}$ that are even more intense than the cyclones in the neutral-shear environment.

Moist processes typically intensify baroclinic development by generating and amplifying low-level PV anomalies through latent heat release (Davis and Emanuel 1991; Balasubramanian and Yau 1994; Schemm et al. 2013). This is the case in the neutral- and barotropic-shear environments, where adding moisture significantly increases the deepening rate, although this effect is much stronger in the neutral-shear case. Yet, decreasing the grid spacing to convection-permitting resolution does not increase the deepening rate in either environment. In contrast, in the low-level-shear environment, the cyclones in the 20-km moist and dry simulations deepen at nearly identical rates through day 6, whereas the cyclone in the 4-km simulation deepens much faster starting at about day 4.

To help explain this discrepancy, Fig. 8 shows the time series of precipitation intensity (measured as the precipitation rate averaged over grid points with nonzero values) and precipitation area (measured as the amount of the domain experiencing nonzero precipitation) for each moist simulation. We hypothesize that cyclones in the neutral-shear environment experience the biggest increase in deepening rate with the addition of moisture because these cyclones produce the most intense precipitation, especially at early times (Fig. 8a). Moist cyclones in the barotropic-shear environment yield much smaller intensities, but the precipitation is much more widespread (Fig. 8b), so the moist cyclones still experience a boost in deepening rate relative to the dry cyclone. In contrast, the moist cyclones in the low-level-shear environment produce precipitation that is less widespread than in the barotropic-shear environment and less intense than in the neutral-shear environment. Thus, the 20-km moist cyclone does not experience a significant increase in the deepening rate relative to the dry cyclone.

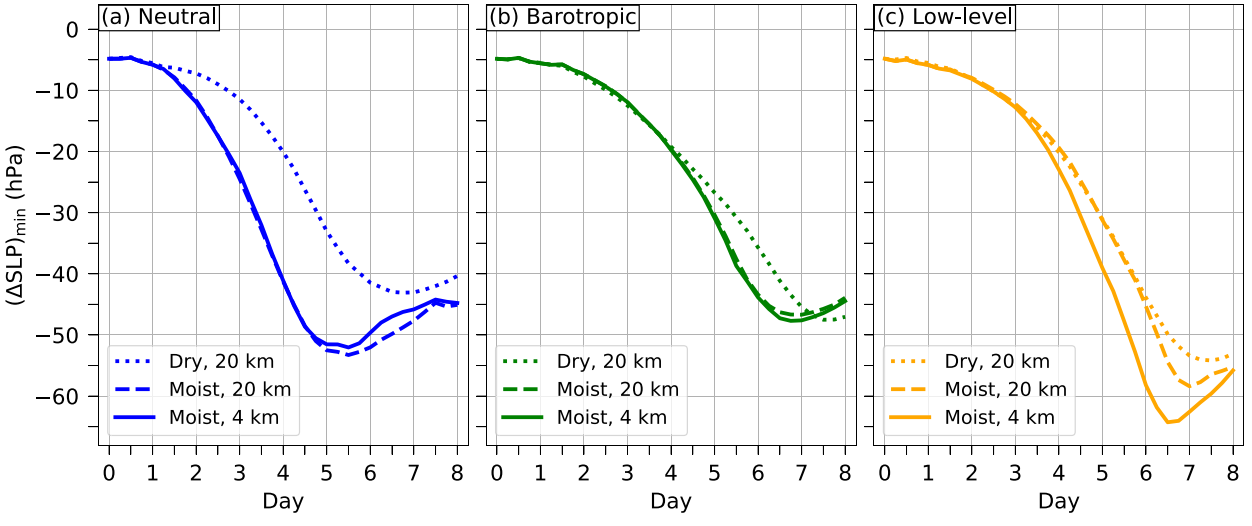

FIG. 7. Time series of $(\Delta SLP)_{min}$ for the simulations in the (a) neutral- (blue), (b) barotropic- (green), and (c) low-level-shear (orange) environments. Solid curves correspond to the 4-km moist simulations. Dashed and dotted curves correspond to the 20-km moist and dry simulations, respectively.

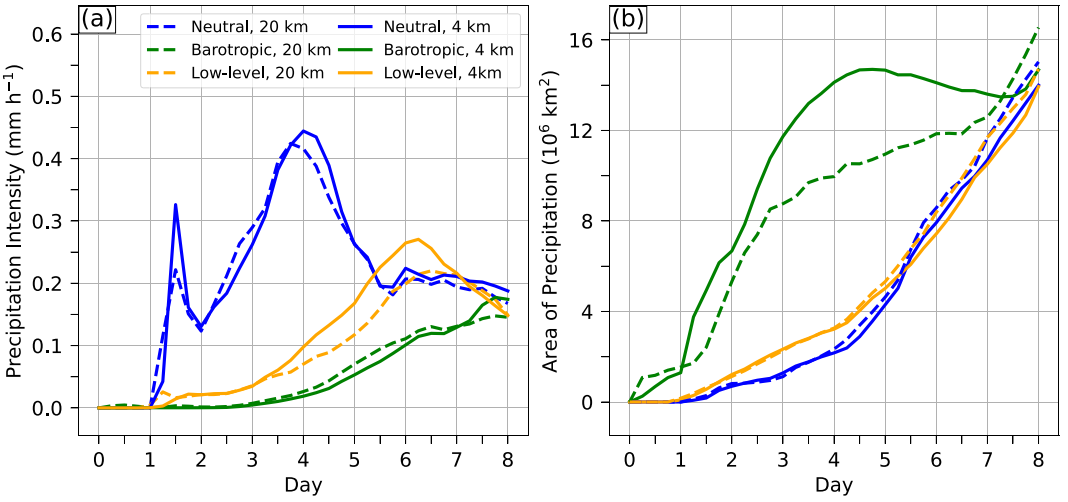

FIG. 8. Time series of (a) precipitation intensity (mm h^{-1}) and (b) area of precipitation (10^6 km^2) for the simulations in the neutral- (blue), barotropic- (green), and low-level-shear (orange) environments. Solid and dashed curves correspond to the 4- and 20-km moist simulations, respectively.

Also, Fig. 9 shows that the relatively high-CAPE air remains well south of the low-pressure centers in the neutral- and barotropic-shear environments, whereas the CAPE is higher and closer to the cyclone in the low-level-shear environment. This may explain why decreasing the grid spacing to convection-permitting resolution significantly increases both the precipitation intensity and the deepening rate in the low-level-shear environment, but not in the neutral- and barotropic-shear environments.

For a more qualitative picture of the moist-baroclinic development in each background state, Figs. 10–12 show snapshots of the surface pressure and modeled composite reflectivity for the 4-km simulations in the neutral-, barotropic-, and low-level-shear environments, respectively. We plot the cyclones during their periods of most rapid deepening (2–5 days in the neutral-shear case and 3–6 days in the barotropic- and low-level-shear cases). For visualization purposes, we plot only a 5000 km × 5000 km subset of the 8000 km × 7200 km domain containing the primary cyclone. We also roll the data by 4000 km in the zonal direction so that the primary cyclone does not straddle the periodic boundary.

The baroclinic development in the neutral-shear environment (Fig. 10) resembles the Shapiro–Keyser conceptual model for cyclogenesis (Shapiro and Keyser 1990), consistent with previous studies that used neutral-shear background states for both dry (Wernli et al. 1998) and moist (Schemm et al. 2013) *f*-plane-channel simulations. At day 2, the cyclone has a minimum central pressure of about 1000 hPa and has already developed a fairly intense, but localized, region of precipitation along the warm front. This region of precipitation

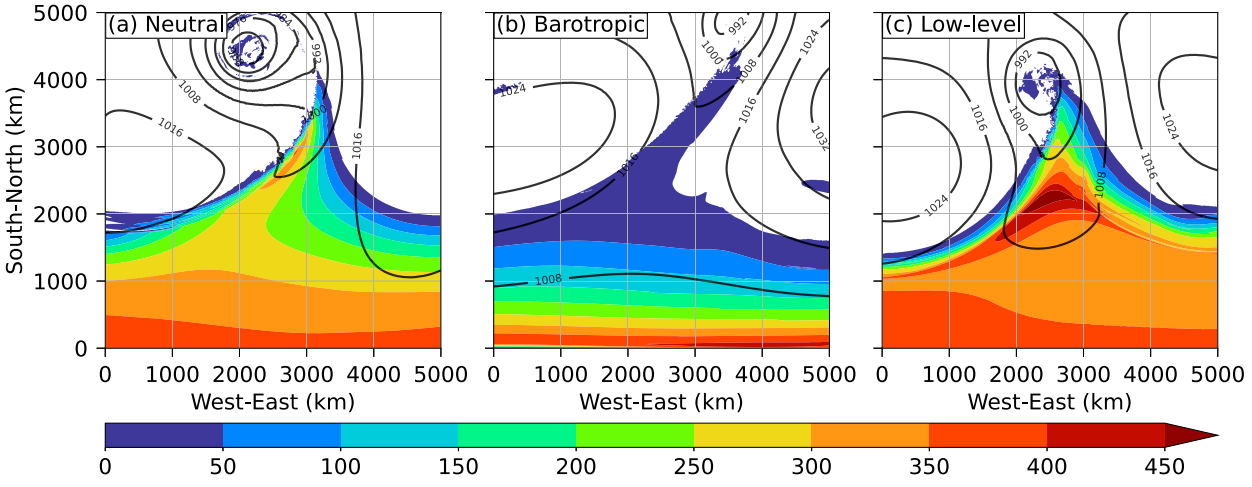

FIG. 9. Surface-based CAPE (color fill every 50 J kg^{-1}) and sea level pressure (black contours every 8 hPa) at day 5 of the 4-km moist simulations in the (a) neutral-, (b) barotropic-, and (c) low-level-shear environments.

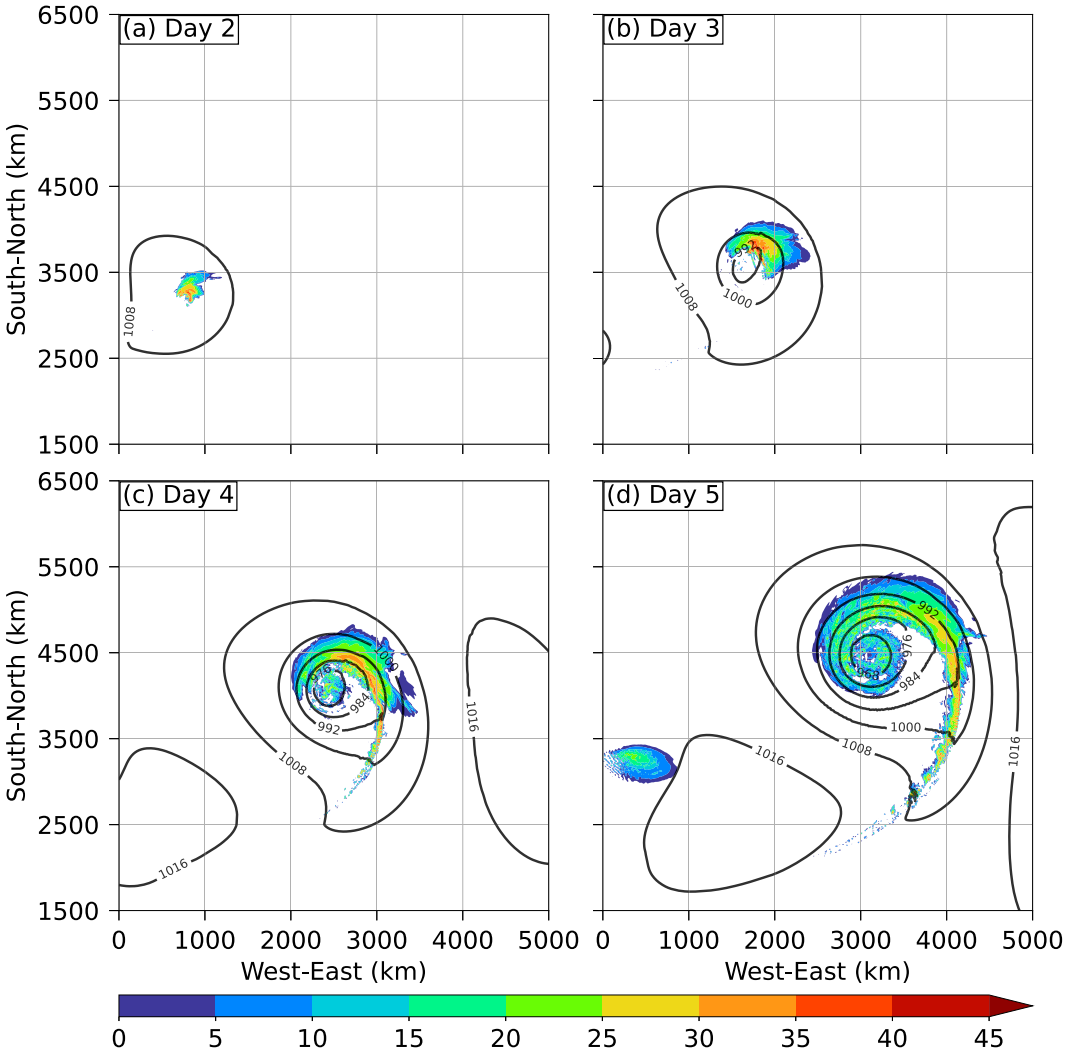

FIG. 10. Modeled composite reflectivity (color fill every 5 dBZ) and sea level pressure (black contours every 8 hPa) at days 2–5 for the 4-km moist simulation in the neutral-shear environment.

intensifies and expands between days 2 and 3 as the low deepens to 989 hPa. The period between days 3 and 4 is characterized by the most rapid deepening, with the low dropping to 971 hPa and very weak anticyclones forming on either side. By day 4, intense precipitation has developed along the cold front and the more widespread region of precipitation has wrapped around a bent-back front, leading to a structure resembling the "T-bone" shape from the Shapiro–Keyser model. The primary cyclone reaches its deepest point of 960 hPa on day 5, at which time lighter, but more widespread, precipitation is wrapping around the low in what appears to be a warm-seclusion process. Also, by day 5, intense precipitation has continued along the cold front, and precipitation has begun to develop in association with a secondary cyclone.

The cyclone in the barotropic-shear environment (Fig. 11), in addition to deepening less rapidly, exhibits a markedly different structure from that of the cyclone in the neutral-shear environment. The baroclinic development is characterized by an elongated cold front, a smaller region of low pressure, and more intense anticyclones, consistent with the dry simulations under anticyclonically sheared conditions from Wernli et al. (1998). At day 3, the low-pressure center does not show a closed isobar despite $(\Delta SLP)_{min}$ being approximately −15 hPa (Fig. 7b); this is because the barotropic-shear environment is characterized by relatively high pressure in the center of the domain (Fig. 4b). At day 3, there is also a substantial, albeit not prototypical-looking, region of precipitation. By day 4, a closed low has formed with a minimum of about 1006 hPa, and more widespread warm-frontal precipitation has developed. By day 5, the low has deepened to 988 hPa and precipitation has begun to develop along the elongated cold front. The most rapid deepening occurs between days 5 and 6, with the low dropping to 967 hPa during this period. At day 6, the cyclone is substantially further north than at a similar period of development

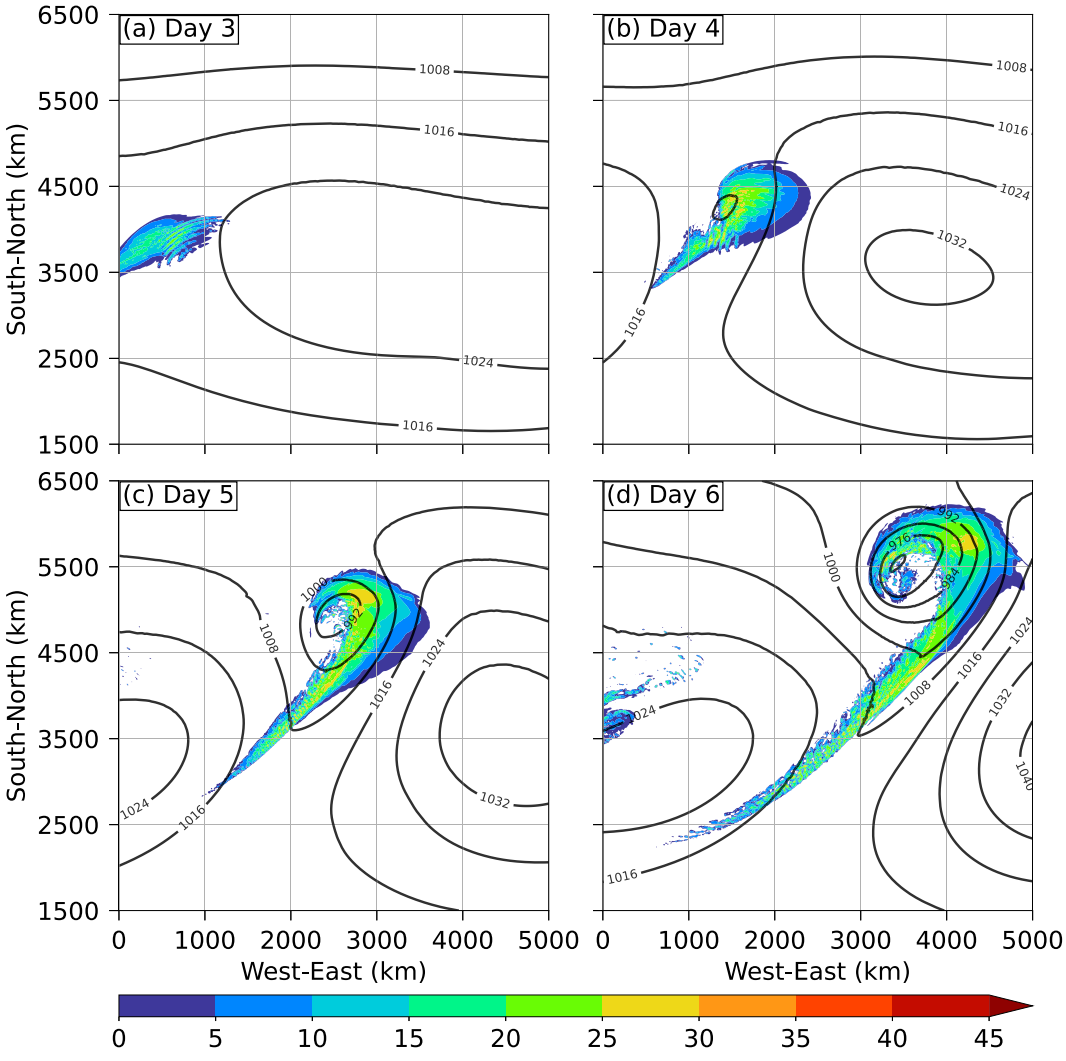

FIG. 11. Modeled composite reflectivity (color fill every 5 dBZ) and sea level pressure (black contours every 8 hPa) at days 3–6 for the 4-km moist simulation in the barotropic-shear environment.

in the neutral-shear environment (cf. Fig. 10d). In addition, the precipitation, albeit less intense, is more widespread in the barotropic-shear environment, particularly along the elongated cold front.

The baroclinic development in the low-level-shear environment (Fig. 12) is more similar to that of the barotropic-shear environment at early times, whereas it is more similar to that of the neutral-shear environment at later times. Since the low-level-shear environment is characterized by high surface pressure in the center of the domain (Fig. 4b), the cyclone is not associated with a closed isobar at day 3, and the flanking anticyclones appear stronger than the closed low that has formed by day 4. These characteristics resemble those of the cyclone's early stages in the barotropic-shear environment. However, at day 5, the cyclone's structure more closely resembles the T-bone shape in the neutral-shear environment, and the precipitation is more localized and more intense than in the barotropic-shear environment. By day 6, the low has deepened to 961 hPa and the widespread region of precipitation has wrapped around the bent-back front; meanwhile, intense precipitation has continued to develop along the cold front. The qualitative similarities between the neutral- and low-level-shear cyclones at later stages may exist because the environments are nearly identical except in the lower troposphere (Figs. 1a,c). Also, as the low-level-shear cyclone develops and propagates northward, it exits the region of anticyclonic shear and enters a region of cyclonic shear (Fig. 4a).

4. Summary

In this paper, we modify a widely used method for generating background states for f-plane-channel simulations so that the environments are more suitable for representing

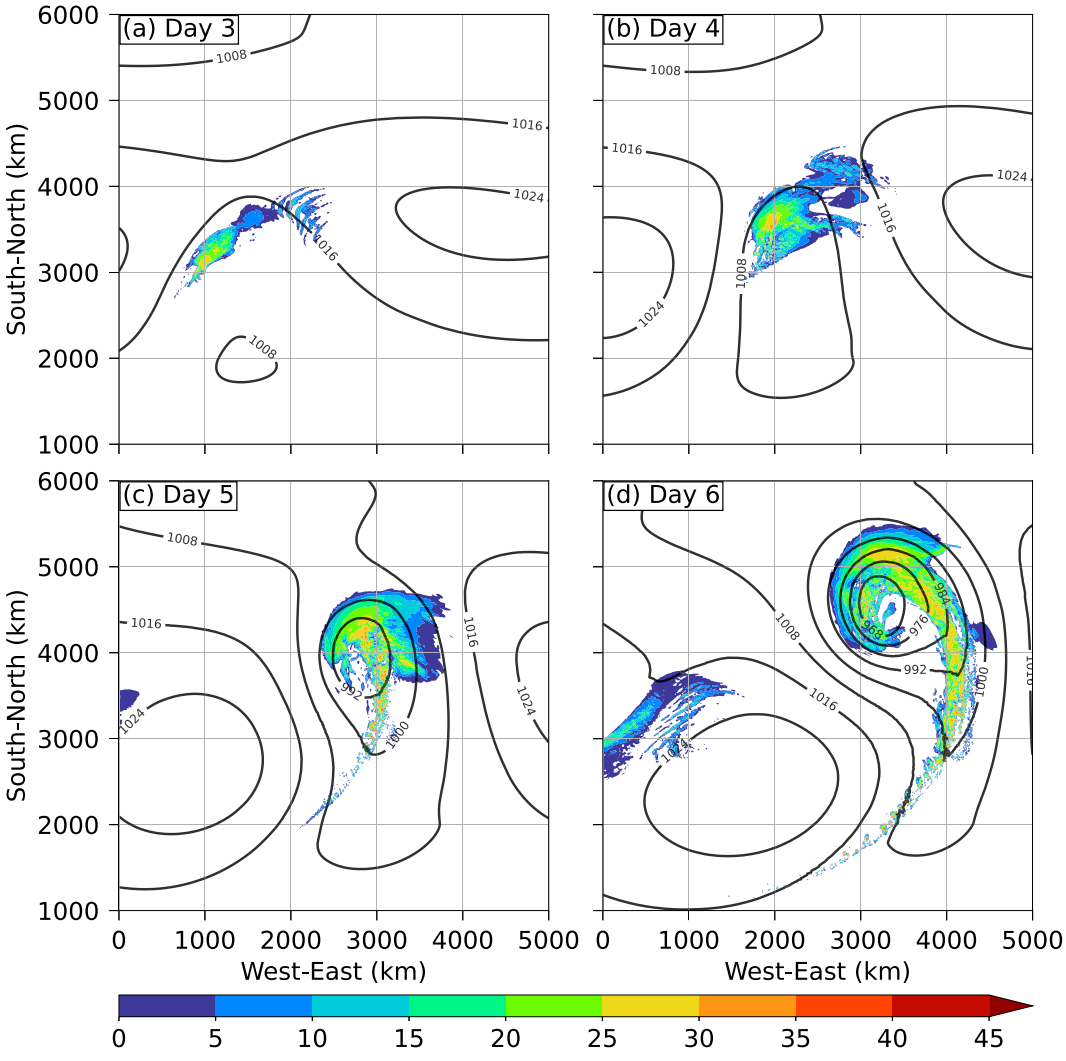

FIG. 12. Modeled composite reflectivity (color fill every 5 dBZ) and sea level pressure (black contours every 8 hPa) at days 3–6 for the 4-km moist simulation in the low-level-shear environment.

moist processes in extratropical cyclones, particularly deep convection. Our method follows the PV-inversion approach of previous studies, but rather than specifying constant PV in the troposphere and the stratosphere, our PV values increase with height in each layer. This modification produces background states with more realistic buoyancy-frequency values, especially near the surface and the tropopause (Fig. 2b). Also, adding moisture to these background states yields lower, more reasonable values of CAPE, and our regula-falsi method for introducing moisture preserves a specified RH distribution while maintaining hydrostatic balance (Fig. 3).

Our method is well suited for studies investigating the sensitivity of extratropical-cyclone processes to changes in the background state. This is because the environment can easily be modified without changing the underlying PV distribution and inadvertently producing implausible values of static stability or CAPE. In other words, our method allows for substantial control over the background state, which comes primarily through the definition of the tropopause in (4). Table 1 depicts the key parameters for changing the tropopause height, shape, and strength (thus modifying the jet and the north–south temperature gradient) and other important aspects of the environment.

Since f-plane-channel simulations without additional horizontal shear produce baroclinic waves with predominantly cyclonic behavior (Balasubramanian and Garner 1997), we provide two options for adding strong anticyclonic horizontal shear and obtaining different baroclinic life cycles. The first approach involves the addition of anticyclonic barotropic shear, while the second involves the modification of the bottom boundary condition in the PV inversion. The first approach is more common (Davies et al. 1991; Balasubramanian and Garner 1997; Wernli et al. 1998), does not alter the

baroclinity, and allows the shear to impact the baroclinic development at all vertical levels. The second approach was introduced by Plougonven and Snyder (2007), and although it preserves the specified PV distribution, it alters the baroclinity, introduces anticyclonic shear only at low levels, and introduces cyclonic shear at the northern and southern edges of the domain.

We demonstrate the characteristics of idealized extratropical cyclones developing in our background states by running 8-day simulations with the WRF Model under different configurations of moisture and horizontal grid spacing. We trigger isolated cyclogenesis in the *f*-plane channel by adding localized QGPV perturbations in the upper troposphere and at the surface. The orientation of these perturbations is favorable for baroclinic development and can be interpreted as Petterssen's type-B cyclogenesis in which an upper-level trough moves over a low-level frontal zone (Petterssen and Smebye 1971). Since the QGPV inversion is independent of the specification of the background state, perturbations of any magnitude, shape, or location can be specified depending on the problem of interest.

The differences between the cyclones developing in the neutral- and barotropic-shear background states are qualitatively similar to those identified by Wernli et al. (1998) in their dry simulations. The development in the neutral-shear environment resembles that of the Shapiro–Keyser conceptual model (Shapiro and Keyser 1990), with a T-bone-like frontal structure and precipitation wrapping around a bent-back front (Fig. 10), whereas the development in the barotropic-shear environment is characterized by widespread precipitation along an elongated cold front, a small region of low pressure, and intense anticyclones (Fig. 11). The addition of moisture increases the rate of cyclone deepening in both environments, although this effect is much stronger in the neutral-shear case. However, the decrease in grid spacing to convection-permitting resolution does not significantly increase the deepening rate or the precipitation intensity in either environment.

The baroclinic development in the low-level-shear environment (Fig. 12) resembles that of the barotropic-shear environment at early times, but more closely resembles that of the neutral-shear environment at later times. In addition, moist cyclones in the low-level-shear environment produce precipitation that is both weaker than in the neutral-shear case and less widespread than in the barotropic-shear case. Consequently, the cyclone deepening rate is not significantly faster, relative to the dry cyclone, in the moist simulation with parameterized convection. Nevertheless, the simulation with explicit convection produces a cyclone with faster deepening rates and greater precipitation intensities, in contrast to the behavior in the neutral- and barotropic-shear environments. We attribute this difference to the larger values of CAPE near the low-pressure center in the low-level-shear environment (Fig. 9), but a more thorough examination of the sensitivity of cyclogenesis to moisture and grid spacing would be a worthwhile avenue for future research.

Acknowledgments. We are grateful for the support of Grant N00014-20-1-2387 from the Office of Naval Research, for computational resources from the Navy Department of Defense Supercomputing Resource Center in Stennis, Mississippi, and for the constructive comments from anonymous reviewers.

Data availability statement. The Python code for generating the initial conditions and the instructions for evolving them in WRF are publicly available at https://github.com/lloverasdan/init-bwave.

APPENDIX A

Sensitivity to RH

The moist simulations considered in the body of this paper have background-state surface RH values of 85%. An important result from section 3 is that the impact of this moisture specification on the cyclone deepening rate relative to the dry simulation depends on the environmental horizontal shear, but does this result also hold for different specifications of the background-state RH? To address this, we use the RH formula given by (8) to generate two additional moist background states in each shear environment with surface RH values of 65% and 75%.

Our method for specifying moisture ensures that the RH is consistent with that specified regardless of the RH distribution. So, our algorithm converges similarly for surface RH values of 65%, 75%, and 85%, as demonstrated by Fig. A1a. Figure A1b shows that the CAPE increases as the surface RH increases. The domain-maximum CAPE is about 35 J kg^{-1} in the 65% environment, about 200 J kg^{-1} in the 75% environment, and about 450 J kg^{-1} in the 85% environment.

We trigger cyclogenesis in the 65% and 75% environments using the same perturbations as for the dry and 85% cases. Figure A2 shows the evolution of cyclone intensity for the 20-km simulations in each shear environment and for each configuration of moisture. The cyclone deepening rate in the neutral-shear environment (Fig. A2a) is slowest for the dry simulation and becomes faster as the RH is increased from 65% to 85%. This behavior is consistent with similar experiments conducted by Schemm et al. (2013, their Fig. 3). In the barotropic-shear environment (Fig. A2b), the cyclone deepening rate also increases as the RH increases from 65% to 85%, but unlike in the neutral-shear case, the 65% cyclone does not deepen faster than the dry cyclone. The cyclone deepening rate is least sensitive to RH in the low-level-shear environment (Fig. A2c), although surprisingly the 75% cyclone deepens slightly faster than even the 85% cyclone between days 4 and 6.

Overall, these results support those from section 3: The sensitivity to the background-state moisture specification is strongest in the neutral-shear environment, is weaker in the barotropic-shear environment, and is weakest in the low-level-shear environment.

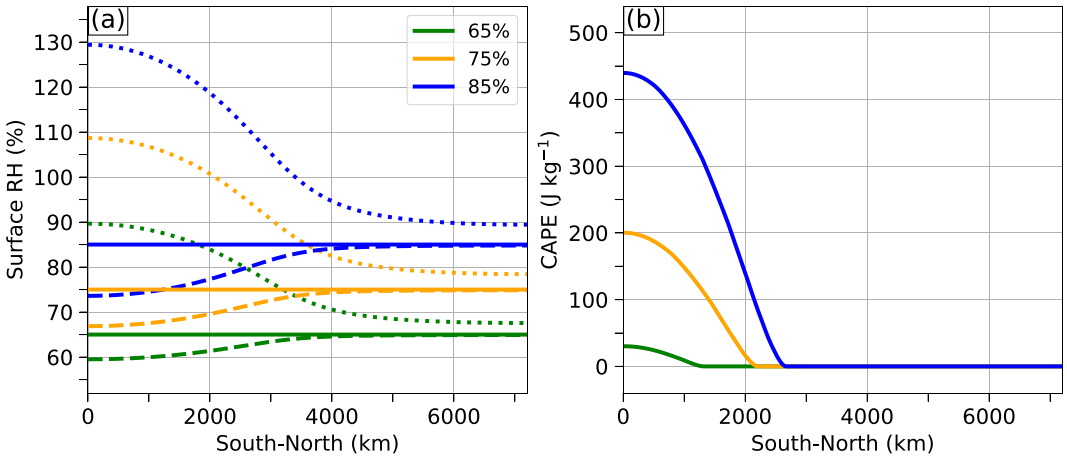

FIG. A1. South–north distributions of (a) surface RH (%) after the first (dotted), second (dashed), and tenth (solid) iterations of our method for specifying moisture and (b) surface-based CAPE (J kg^{-1}) after the 10th iteration for the neutral-shear environments with surface RHs of 65% (green), 75% (orange), and 85% (blue).

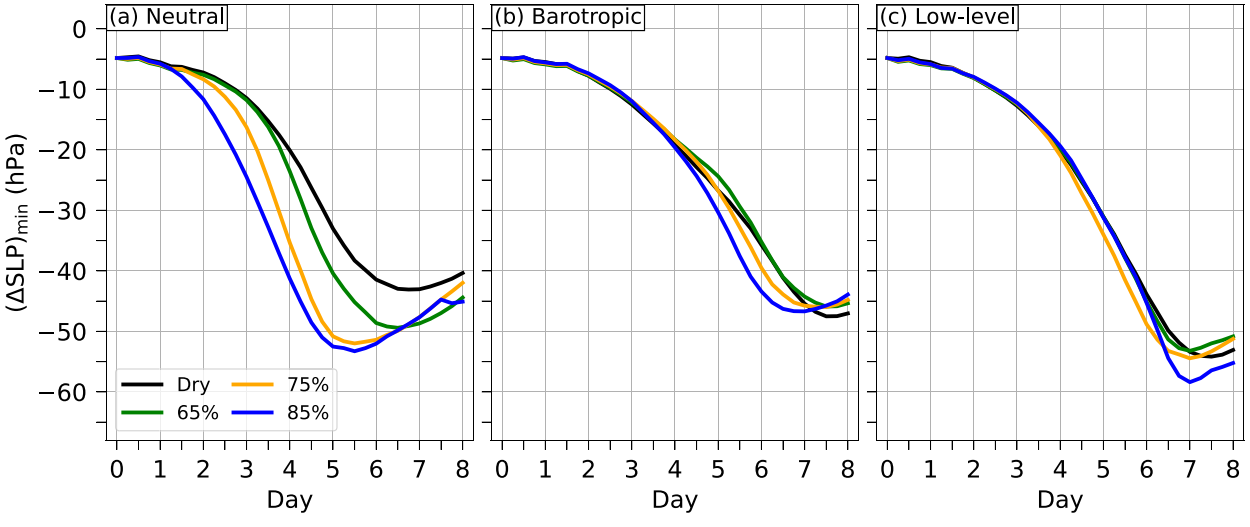

FIG. A2. Time series of $(\Delta SLP)_{min}$ for the 20-km dry (black) and moist simulations with surface RHs of 65% (green), 75% (orange), and 85% (blue) in the (a) neutral-, (b) barotropic-, and (c) low-level-shear environments.

APPENDIX B

PV Formula

The specified PV distribution for the baroclinically unstable background state is of the form:

$$\mathrm{PV}[\Pi_{\mathrm{tp}}(y), \Pi] = \frac{1}{2}(a\mathrm{PV}_t + b\mathrm{PV}_s) + \frac{1}{2}(a\mathrm{PV}_t - b\mathrm{PV}_s)\tanh\left(2\frac{\Pi - \Pi_{\mathrm{tp}}}{\Delta\Pi_d}\right), \quad \text{(B1)}$$

where $\mathrm{PV}_t = 0.2$ PVU (1 PVU $= 10^{-6}$ K kg^{-1} m^2 is the reference tropospheric PV, $\mathrm{PV}_s = 7.0$ PVU is the reference stratospheric PV, $\Delta\Pi_d = 15$ J K^{-1} kg^{-1} is the depth of the tropopause layer, and the parameters a and b determine the rate of PV increase in the troposphere and stratosphere, respectively,

$$a[\Pi_{\mathrm{tp}}(y), \Pi] = \begin{cases} 1 + 5\left(\dfrac{\Pi_{\mathrm{bot}} - \Pi}{\Pi_{\mathrm{bot}} - \Pi_{\mathrm{tp}}}\right)^2, & \text{if } \Pi \geq \Pi_{\mathrm{tp}}, \\ 1, & \text{if } \Pi < \Pi_{\mathrm{tp}}, \end{cases} \quad \text{and} \quad \text{(B2)}$$

$$b[\Pi_{\mathrm{tp}}(y), \Pi] = \begin{cases} 1, & \text{if } \Pi \geq \Pi_{\mathrm{tp}}, \\ 1 + 3\left(\dfrac{\Pi_{\mathrm{tp}} - \Pi}{\Pi_{\mathrm{tp}} - \Pi_{\mathrm{top}}}\right)^3, & \text{if } \Pi < \Pi_{\mathrm{tp}}. \end{cases} \quad \text{(B3)}$$

APPENDIX C

Numerical Details for the PV Inversion

We invert the specified PV distribution by solving (1) for ϕ with centered second-order finite-difference approximations for the derivatives:

$$\left(\frac{\partial^2\phi}{\partial y^2}\right)_{j,k} \approx \frac{\phi_{j+1,k} - 2\phi_{j,k} + \phi_{j-1,k}}{(\Delta y)^2}, \quad \text{(C1)}$$

$$\left(\frac{\partial^2\phi}{\partial \Pi^2}\right)_{j,k} \approx \frac{\phi_{j,k+1} - 2\phi_{j,k} + \phi_{j,k-1}}{(\Delta\Pi)^2}, \quad \text{and} \quad \text{(C2)}$$

$$\left[\frac{\partial^2\phi}{(\partial y \partial \Pi)}\right]_{j,k} \approx \frac{\phi_{j+1,k+1} - \phi_{j+1,k-1} - \phi_{j-1,k+1} + \phi_{j-1,k-1}}{4(\Delta y \Delta\Pi)}, \quad \text{(C3)}$$

where j and k represent grid indices in the y and Π directions, respectively, and Δy and $\Delta\Pi$ are the grid spacings. Substituting (C1)–(C3) into (1) yields a quadratic equation to solve for each $\phi_{j,k}$:

$$\phi_{j,k}^2 + b\phi_{j,k} + c = 0, \quad \text{(C4)}$$

where

$$b = -\frac{1}{2}[\phi_{j+1,k} + \phi_{j-1,k} + \phi_{j,k+1} + \phi_{j,k-1} + (f_0\Delta y)^2], \quad \text{and} \quad \text{(C5)}$$

$$c = -\frac{1}{4}\Big[\mathrm{PV}_{j,k}\Pi_k^{-(1-1/\kappa)}(\Delta y\Delta\Pi)^2 f_0 p_0 (g\kappa)^{-1} c_p^{-1/\kappa} + \frac{1}{16}(\phi_{j+1,k+1} - \phi_{j-1,k+1} - \phi_{j+1,k-1} + \phi_{j-1,k-1})^2 - (\phi_{j+1,k} + \phi_{j-1,k})(\phi_{j,k+1} + \phi_{j,k-1}) - (f_0\Delta y)^2(\phi_{j,k+1} + \phi_{j,k-1})\Big]. \quad \text{(C6)}$$

We arrive at the solution using a successive overrelaxation method with 50 000 iterations. We do not employ a convergence criterion. At each iteration n and at each grid point (j, k), we compute $\phi_{j,k}^*$ by solving (C4):

$$\phi_{j,k}^* = \frac{1}{2}(-b - |b^2 - 4c|^{1/2}), \quad \text{(C7)}$$

and before moving onto the next grid point, we update the solution as

$$\phi_{j,k}^n = \phi_{j,k}^{n-1} + 1.8(\phi_{j,k}^* - \phi_{j,k}^{n-1}). \quad \text{(C8)}$$

At each iteration [i.e., after evaluating (C8) for each internal grid point], we apply the boundary conditions: $\partial\phi/\partial y = 0$ at the northern and southern boundaries, the moist potential temperature at the top boundary $\theta_{m_{\mathrm{top}}} = \partial\phi_{\mathrm{top}}/\partial\Pi_{\mathrm{top}}$, and the geopotential at the bottom boundary ϕ_{bot}. We first run this solver on a low-resolution mesh to arrive at an initial guess for the solver on the full mesh.

APPENDIX D

QGPV Inversion of the Cyclogenetic Perturbations

To invert the cyclogenetic perturbations, we solve the Boussinesq, f-plane form of the QGPV equation in three-dimensional Cartesian coordinates with $(L_x, L_y, L_z) = (8000\ \mathrm{km}, 7200\ \mathrm{km}, 20\ \mathrm{km})$:

$$q = f_0 + \frac{\partial^2\psi}{\partial x^2} + \frac{\partial^2\psi}{\partial y^2} + \frac{\partial}{\partial z}\left(\frac{f_0^2}{N_r^2}\frac{\partial\psi}{\partial z}\right), \quad \text{(D1)}$$

where $\psi = p'/(\rho_0 f_0)$ is the QG streamfunction, p' is the QG pressure perturbation, $\rho_0 = 1.0$ kg m^{-3} is the reference density, $N_r^2 = (g/\theta_r)(\partial\theta_r/\partial z)$, and $\theta_r(z)$ is the U.S. standard atmosphere for potential temperature (COESA 1976). Taking $q' = q - f_0$ and assuming that $\partial N_r/\partial z$ is negligible (a reasonable assumption for the troposphere), we can rewrite (D1) as

$$q' = \frac{\partial^2\psi}{\partial x^2} + \frac{\partial^2\psi}{\partial y^2} + \frac{f_0^2}{N_r^2}\frac{\partial^2\psi}{\partial z^2}. \quad \text{(D2)}$$

To solve (D2), we assume wave-like solutions in the horizontal direction:

$$\psi(x, y, z) = \psi(z)e^{i(kx - ly)}, \quad \text{and} \quad \text{(D3)}$$

$$q'(x, y, z) = q'(z)e^{i(kx - ly)}, \quad \text{(D4)}$$

where k is the zonal wavenumber and l is the meridional wavenumber. Substituting (D3) and (D4) into (D2) results in a differential equation to solve for $\psi(z)$ at each spectral grid point (k, l):

$$b(z)\frac{\partial^2\psi}{\partial z^2} - K^2\psi(z) = q'(z), \tag{D5}$$

where $b(z) = f_0^2/N_r^2$ and $K^2 = k^2 + l^2$. At the top boundary, we set $\psi_{\text{top}} = 0\ \text{m}^2\ \text{s}^{-1}$, and at the surface, we specify $\partial\psi_{\text{bot}}/\partial z$, which via hydrostatic balance is proportional to $\theta'_{m_{\text{bot}}}$.

If we use a centered second-order finite-difference approximation with uniform grid spacing Δz,

$$\left(\frac{\partial^2\psi}{\partial z^2}\right)_k \approx \frac{\psi_{k+1} - 2\psi_k + \psi_{k-1}}{(\Delta z)^2}, \tag{D6}$$

we can write (D5) in matrix form as $\mathbf{A\Psi} = \mathbf{Q}'$, where

$$\mathbf{A} = \frac{1}{(\Delta z)^2}\begin{bmatrix} -(K\Delta z)^2 - b_1 & b_1 & & & \\ b_2 & -(K\Delta z)^2 - 2b_2 & b_2 & & \\ & \ddots & \ddots & \ddots & \\ & & b_{n-1} & -(K\Delta z)^2 - 2b_{n-1} & b_{n-1} \\ & & & b_n & -(K\Delta z)^2 - 2b_n \end{bmatrix}, \tag{D7}$$

$$\mathbf{\Psi} = \begin{bmatrix} \psi_1 \\ \psi_2 \\ \vdots \\ \psi_n \end{bmatrix}, \quad \text{and} \tag{D8}$$

$$\mathbf{Q}' = \begin{bmatrix} q'_1/2 + (b_1/\Delta z)\partial\psi_{\text{bot}}/\partial z \\ q'_2 \\ \vdots \\ q'_n \end{bmatrix}. \tag{D9}$$

To invert the QGPV perturbations, we transform q' and $\theta'_{m_{\text{bot}}}$ into Fourier space, solve $\mathbf{A\Psi} = \mathbf{Q}'$ for each (k, l), transform the solution ψ into Cartesian space, and compute the pressure, geostrophically balanced wind, and hydrostatically balanced moist-potential-temperature perturbations as

$$p' = \rho_0 f_0 \psi, \tag{D10}$$

$$u' = -\frac{\partial\psi}{\partial y}, \tag{D11}$$

$$v' = \frac{\partial\psi}{\partial x}, \quad \text{and} \tag{D12}$$

$$\theta'_m = \frac{f_0\theta_r}{g}\frac{\partial\psi}{\partial z}. \tag{D13}$$

REFERENCES

Balasubramanian, G., and M. K. Yau, 1994: The effects of convection on a simulated marine cyclone. *J. Atmos. Sci.*, **51**, 2397–2417, https://doi.org/10.1175/1520-0469(1994)051<2397:TEOCOA>2.0.CO;2.

——, and S. T. Garner, 1997: The role of momentum fluxes in shaping the life cycle of a baroclinic wave. *J. Atmos. Sci.*, **54**, 510–533, https://doi.org/10.1175/1520-0469(1997)054<0510:TROMFI>2.0.CO;2.

Birner, T., A. Dörnbrack, and U. Schumann, 2002: How sharp is the tropopause at midlatitudes? *Geophys. Res. Lett.*, **29**, 1700, https://doi.org/10.1029/2002GL015142.

Bolton, D., 1980: The computation of equivalent potential temperature. *Mon. Wea. Rev.*, **108**, 1046–1053, https://doi.org/10.1175/1520-0493(1980)108%3C1046:TCOEPT%3E2.0.CO;2.

COESA, 1976: U.S. Standard Atmosphere, 1976. NOAA Tech. Memo. NOAA-S/T-76-1562, 243 pp., https://ntrs.nasa.gov/citations/19770x009539.

Davies, H. C., C. Schär, and H. Wernli, 1991: The palette of fronts and cyclones within a baroclinic wave development. *J. Atmos. Sci.*, **48**, 1666–1689, https://doi.org/10.1175/1520-0469(1991)048<1666:TPOFAC>2.0.CO;2.

Davis, C. A., and K. A. Emanuel, 1991: Potential vorticity diagnostics of cyclogenesis. *Mon. Wea. Rev.*, **119**, 1929–1953, https://doi.org/10.1175/1520-0493(1991)119<1929:PVDOC>2.0.CO;2.

Eady, E. T., 1949: Long waves and cyclone waves. *Tellus*, **1** (3), 33–52, https://doi.org/10.3402/tellusa.v1i3.8507.

Hong, S.-Y., Y. Noh, and J. Dudhia, 2006: A new vertical diffusion package with an explicit treatment of entrainment processes. *Mon. Wea. Rev.*, **134**, 2318–2341, https://doi.org/10.1175/MWR3199.1.

Hoskins, B. J., and N. V. West, 1979: Baroclinic waves and frontogenesis. Part II: Uniform potential vorticity jet flows-cold and warm fronts. *J. Atmos. Sci.*, **36**, 1663–1680, https://doi.org/10.1175/1520-0469(1979)036%3C1663:BWAFPI%3E2.0.CO;2.

Jiménez, P. A., J. Dudhia, J. F. González-Rouco, J. Navarro, J. P. Montávzez, and E. García-Bustamente, 2012: A revised scheme for the WRF surface layer formulation. *Mon. Wea. Rev.*, **140**, 898–918, https://doi.org/10.1175/MWR-D-11-00056.1.

Kain, J. S., 2004: The Kain–Fritsch convective parameterization: An update. *J. Appl. Meteor.*, **43**, 170–181, https://doi.org/10.1175/1520-0450(2004)043<0170:TKCPAU>2.0.CO;2.

Kirshbaum, D. J., T. M. Merlis, J. R. Gyakum, and R. McTaggart-Cowan, 2018: Sensitivity of idealized moist baroclinic waves to

environmental temperature and moisture content. *J. Atmos. Sci.*, **75**, 337–360, https://doi.org/10.1175/JAS-D-17-0188.1.

Klemp, J. B., J. Dudhia, and A. D. Hassiotis, 2008: An upper gravity-wave absorbing layer for NWP applications. *Mon. Wea. Rev.*, **136**, 3987–4004, https://doi.org/10.1175/2008MWR2596.1.

Lloveras, D. J., L. H. Tierney, and D. R. Durran, 2022: Mesoscale predictability in moist midlatitude cyclones is not sensitive to the slope of the background kinetic energy spectrum. *J. Atmos. Sci.*, **79**, 119–139, https://doi.org/10.1175/JAS-D-21-0147.1.

——, D. R. Durran, and J. D. Doyle, 2023: The two- to four-day predictability of midlatitude cyclones: Don't sweat the small stuff. *J. Atmos. Sci.*, **80**, 2613–2633, https://doi.org/10.1175/JAS-D-22-0232.1.

Mansell, E. R., C. L. Ziegler, and E. C. Bruning, 2010: Simulated electrification of a small thunderstorm with two-moment bulk microphysics. *J. Atmos. Sci.*, **67**, 171–194, https://doi.org/10.1175/2009JAS2965.1.

Menchaca, M. Q., and D. R. Durran, 2017: Mountain waves, downslope winds, and low-level blocking forced by a midlatitude cyclone encountering an isolated ridge. *J. Atmos. Sci.*, **74**, 617–639, https://doi.org/10.1175/JAS-D-16-0092.1.

Norris, J., G. Vaughan, and D. M. Schultz, 2014: Precipitation banding in idealized baroclinic waves. *Mon. Wea. Rev.*, **142**, 3081–3099, https://doi.org/10.1175/MWR-D-13-00343.1.

——, ——, and ——, 2017: Variability of precipitation along cold fronts in idealized baroclinic waves. *Mon. Wea. Rev.*, **145**, 2971–2992, https://doi.org/10.1175/MWR-D-16-0409.1.

Nuss, W. A., and R. A. Anthes, 1987: A numerical investigation of low-level processes in rapid cyclogenesis. *Mon. Wea. Rev.*, **115**, 2728–2743, https://doi.org/10.1175/1520-0493(1987)115<2728:ANIOLL>2.0.CO;2.

Olson, J. B., and B. A. Colle, 2007: A modified approach to initialize an idealized extratropical cyclone within a mesoscale model. *Mon. Wea. Rev.*, **135**, 1614–1624, https://doi.org/10.1175/MWR3364.1.

Petterssen, S., and S. J. Smebye, 1971: On the development of extratropical cyclones. *Quart. J. Roy. Meteor. Soc.*, **97**, 457–482, https://doi.org/10.1002/qj.49709741407.

Plougonven, R., and C. Snyder, 2007: Inertia–gravity waves spontaneously generated by jets and fronts. Part I: Different baroclinic life cycles. *J. Atmos. Sci.*, **64**, 2502–2520, https://doi.org/10.1175/JAS3953.1.

Rotunno, R., W. C. Skamarock, and C. Snyder, 1994: An analysis of frontogenesis in numerical simulations of baroclinic waves. *J. Atmos. Sci.*, **51**, 3373–3398, https://doi.org/10.1175/1520-0469(1994)051%3C3373:AAOFIN%3E2.0.CO;2.

Schemm, S., H. Wernli, and L. Papritz, 2013: Warm conveyor belts in idealized moist baroclinic wave simulations. *J. Atmos. Sci.*, **70**, 627–652, https://doi.org/10.1175/JAS-D-12-0147.1.

Shapiro, M. A., and D. Keyser, 1990: Fronts, jet streams and the tropopause. *Extratropical Cyclones: The Erik Palmén Memorial Volume*, C. W. Newton and E. O. Holopainen, Eds., Amer. Meteor. Soc., 167–191, https://doi.org/10.1007/978-1-944970-33-8_10.

Skamarock, W. C., and Coauthors, 2008: A description of the Advanced Research WRF version 3. NCAR Tech. Note NCAR/TN-475+STR, 113 pp., https://doi.org/10.5065/D68S4MVH.

Sun, Y. Q., and F. Zhang, 2016: Intrinsic versus practical limits of atmospheric predictability and the significance of the butterfly effect. *J. Atmos. Sci.*, **73**, 1419–1438, https://doi.org/10.1175/JAS-D-15-0142.1.

Tan, Z.-M., F. Zhang, R. Rotunno, and C. Snyder, 2004: Mesoscale predictability of moist baroclinic waves: Experiments with parameterized convection. *J. Atmos. Sci.*, **61**, 1794–1804, https://doi.org/10.1175/1520-0469(2004)061<1794:MPOMBW>2.0.CO;2.

Terpstra, A., and T. Spengler, 2015: An initialization method for idealized channel simulations. *Mon. Wea. Rev.*, **143**, 2043–2051, https://doi.org/10.1175/MWR-D-14-00248.1.

Thorncroft, C. D., B. J. Hoskins, and M. E. McIntyre, 1993: Two paradigms of baroclinic-wave life-cycle behaviour. *Quart. J. Roy. Meteor. Soc.*, **119**, 17–55, https://doi.org/10.1002/qj.49711950903.

Waite, M. L., and C. Snyder, 2013: Mesoscale energy spectra of moist baroclinic waves. *J. Atmos. Sci.*, **70**, 1242–1256, https://doi.org/10.1175/JAS-D-11-0347.1.

Weisman, M. L., W. C. Skamarock, and J. B. Klemp, 1997: The resolution dependence of explicitly modeled convective systems. *Mon. Wea. Rev.*, **125**, 527–548, https://doi.org/10.1175/1520-0493(1997)125%3C0527:TRDOEM%3E2.0.CO;2.

Wernli, H., R. Fehlmann, and D. Lüthi, 1998: The effect of barotropic shear on upper-level induced cyclogenesis: Semigeostrophic and primitive equation numerical simulations. *J. Atmos. Sci.*, **55**, 2080–2094, https://doi.org/10.1175/1520-0469(1998)055<2080:TEOBSO>2.0.CO;2.

Zhang, F., 2004: Generation of mesoscale gravity waves in upper-tropospheric jet–front systems. *J. Atmos. Sci.*, **61**, 440–457, https://doi.org/10.1175/1520-0469(2004)061<0440:GOMGWI>2.0.CO;2.

——, N. Bei, R. Rotunno, C. Snyder, and C. C. Epifanio, 2007: Mesoscale predictability of moist baroclinic waves: Convection-permitting experiments and multistage error growth dynamics. *J. Atmos. Sci.*, **64**, 3579–3594, https://doi.org/10.1175/JAS4028.1.